

Dents in the Veil: Protostellar feedback in Orion

Ü. Kavak^{1,2,3,4}, J. Bally⁵, J. R. Goicoechea⁶, C. H. M. Pabst^{4,6}, F. F. S. van der Tak^{2,1}, and A. G. G. M. Tielens⁴

¹ Kapteyn Astronomical Institute, University of Groningen, P.O. Box 800, 9700 AV Groningen, The Netherlands
e-mail: ukavak@sofia.usra.edu

² SRON Netherlands Institute for Space Research, Landleven 12, 9747 AD Groningen, The Netherlands

³ SOFIA Science Center, USRA, NASA Ames Research Center, M.S. N232-12, Moffett Field, CA 94035, USA

⁴ Leiden Observatory, Leiden University, PO Box 9513, NL-2300RA, Leiden, the Netherlands

⁵ Department of Astrophysical and Planetary Sciences, University of Colorado, Boulder, Colorado 80389, USA

⁶ Instituto de Física Fundamental, CSIC, Calle Serrano 121-123, 28006 Madrid, Spain

Received Month XX, 2021; accepted Month XX, 2021

ABSTRACT

Context. Interest in stellar feedback has recently increased because new studies suggest that radiative and mechanical feedback from young massive stars regulate the physical and chemical composition of the interstellar medium (ISM) significantly. Recent SOFIA [C II] 158 μm observations of the Orion Veil revealed that the expanding bubble is powered by stellar winds and influenced by previously active molecular outflows of ionizing massive stars.

Aims. We aim to investigate the mechanical feedback on the whole Veil shell by searching for jets/outflows interacting with the Veil shell and determining the origin/driving mechanisms of these collisions.

Methods. We make use of the [C II] 158 μm map of the Orion Nebula taken with the upGREAT instrument onboard SOFIA. We image the [C II] emission the more extreme local standard of rest velocities (v_{LSR}) between -3 and -20 km s^{-1} to pinpoint the high-velocity structures. Using position-velocity (PV) diagrams and high-velocity [C II] emission, we search for spots of shock-accelerated [C II] emitting gas, so called *dents*. At these positions, we extract [C II] line profiles to identify velocity components. We also compare the intensity distribution of the [C II] emission with that of 8 μm PAH and 70 μm warm dust emission to see if there is a trend among these PDR tracers and to understand the origin of the dents.

Results. We identify six dents on the Veil shell with sizes between 0.3 and 1.35 pc and expansion velocities ranging from 4 to 14 km s^{-1} relative to the expanding Veil shell. The [C II] line widths toward the dents vary from 4 to 16 km s^{-1} indicating that the dents are the result of interaction of highly turbulent motions (e.g., shocked gas) with the Veil shell. Moreover, dents appear only in the [C II] PV diagram but not in the ^{12}CO or H I 21 cm diagrams. Furthermore, the intensity distribution of the [C II] emission of the dents has a tight correlation with that of 8 μm and 70 μm as long as the OMC or the Veil do not dominate its emission. Also, the observed dents do not have CO counterpart emission. These results indicate that the dents are made up of CO-dark H_2 gas. In the light of these findings, as well as the momenta of the dents and their dynamical timescales, we propose that the dents are created by the interaction of collimated jets/outflows from protostars with luminosities ranging from 10^3 to $10^4 L_{\odot}$ indicating B-type stars in the Orion star-forming cloud with the surrounding Veil shell. However, it is challenging to pinpoint the driving stars as they may have moved from the original ejection points of the jets/outflows.

Conclusions. We conclude that the dynamics of the expanding Veil shell is influenced not just by the O-type stars in the Trapezium cluster, but also by less massive stars, especially B-type, in the Orion Nebula. Mechanical feedback from protostars with a range of masses appears to play an important role in determining the morphology of H II regions and injecting turbulence into the medium.

Key words. Stars: massive – ISM: bubbles – ISM: kinematics and dynamics

1. Introduction

Interest in massive stars (with luminosities larger than $10^3 L_{\odot}$, corresponding to a spectral type of B3 or earlier, and stellar masses higher than $8 M_{\odot}$ (Tan et al. 2014)) has increased in the last three decades as they inject considerable energy and momentum to unbind and disperse their natal clouds via stellar winds, powerful outflows, ionising radiation, and supernova explosions (Krumholz et al. 2014; Bally 2016; Motte et al. 2018). The injection of mass, momentum, and energy which is called ‘stellar feedback’ can be seen on various spatial scales (from ~ 1 to ~ 100 pc) and dynamical timescales (from 10^4 to 10^6 years). At first glance, supernova explosions are the most energetic feedback process delivering immense energy (on the order of 10^{51} erg seen in observations) that can reshape the morphology and composition of star-forming galaxies on large scales

(10–100 pc) (Thielemann et al. 2011). However, recent studies reveal that feedback via protostellar outflows is also vital in setting the observed properties such as masses of stars (Olivier et al. 2021; Guszejnov et al. 2021).

In contrast to their low-mass companions, massive stars reach their main-sequence luminosity while still embedded and accreting in a natal cloud of gas and dust due to their shorter Kelvin-Helmholtz timescales (Zinnecker & Yorke 2007). Protostars of all masses eject energetic jets/outflows to remove the angular momentum excess from the accretion process till they reach the main-sequence (Beuther et al. 2002; Sánchez-Monge et al. 2013; Kavak et al. 2021). This results in the entrainment of a significant amount of ambient molecular material. Even after the jets/outflows switch off when the star reaches the zero-age main sequence (ZAMS), relics of previously active molecular outflows, in other words fossil outflows, will continue to expand

on their velocity vector and interact with the surrounding environment (Quillen et al. 2005). Furthermore, massive stars tend to form in dense clusters and exhibit a high multiplicity fraction (Motte et al. 2018). Therefore, it is possible to find newly forming massive stars and their outflows in the same cluster (O’Dell et al. 2015) while other massive stars are already on the main sequence and radiate strong UV radiation (as in the Orion Nebula; Bally 2016). From the observational point of view, quantifying the relative contribution of stellar feedback before and after reaching the ZAMS has been challenging for years (Lopez et al. 2011), despite the fact that state-of-the-art simulations are capable of employing stellar feedback modes individually (Walch et al. 2012; Haid et al. 2018; Grudić et al. 2021).

Orion’s Veil (Veil for short), which is a series of foreground layers (e.g., 9 layers identified by Abel et al. 2019) of gas and dust lying in front of the Trapezium stars (O’Dell 2018), is a unique laboratory for studying the relative effects of feedback mechanisms because its proximity allows us to resolve the bubbles in the Orion Molecular Cloud (OMC) spatially and in Doppler velocity space (O’Dell et al. 2011). The [C II] emitting Veil layer is a thin (0.5 pc) neutral and predominantly atomic shell (Abel et al. 2016; Goicoechea et al. 2020) expanding at a velocity of 13 km s^{-1} toward us from the OMC-1 core driven by the kinetic energy converted from stellar winds of θ^1 Ori C, the most ionizing star in the Orion Nebula (O’Dell 2001; Pabst et al. 2019). Some studies suggest a multi-layered structure model for the Veil based on the velocity components characterized through the emission and absorption lines (Abel et al. 2016; O’Dell 2018; Abel et al. 2019). The main emission component of the Veil is traced by [C II] fine-structure transition ($^2P_{3/2} \rightarrow ^2P_{1/2}$ at $158 \mu\text{m}$ or 1.9 THz , i.e., $\Delta E/k_B = 91.2 \text{ K}$), which is the main cooling agent of neutral interstellar gas. While there are other tracers of CO-dark H_2 gas (e.g., $\text{HF } J=1-0$; Kavak et al. 2019), [C II] is by far the brightest as C^+ is the dominant carbon bearing species and the line is readily excited. Velocity-resolved [C II] line observations are the state-of-the-art technique in determining the driving mechanisms of feedback in massive star-forming regions (Goicoechea et al. 2015; Seo et al. 2019; Pabst et al. 2019, 2020; Schneider et al. 2020; Tiwari et al. 2021; Luisi et al. 2021).

Not only photoionization radiation from θ^1 Ori C, but high-velocity structures such as jets/outflows from YSOs and Herbig-Haro objects play a role in the dynamics of the Veil on various scales (Henney et al. 2007; Bally et al. 2006; O’Dell et al. 1997). Recently, Kavak et al. (2022) showed that even relics of previously active molecular outflows (i.e., fossil outflows) from θ^1 Ori C affect the morphology of the Veil. Blue-shifted ejections, which have relatively weak [O III] emission, are impinging on the neutral foreground Veil shell (HH 202, HH 269, HH 203+204; O’Dell 2001) as the Veil itself expands. The collision of such objects with the Veil shell are a plausible explanation for the large temperature gradients (Peimbert et al. 1991). In this work, we investigate high velocity structures seen in the [C II] observations using PV diagrams generated in cuts along the Veil and search for an association with shock accelerated atomic gas. Furthermore, we attempt to investigate the origin of the shock-accelerated gas¹ by estimating its momentum and dynamical timescale.

We organize the paper as follows. In Section 2 we describe the [C II], ^{12}CO and ^{13}CO , and mid- and far-IR observations of the Veil. In Section 3, we describe our methods to identify the

¹ We use the term of *dent* for the shock accelerated gas because the shocks collide with the inner surface of the Veil, resulting in hollow-like structures on the Veil’s surface.

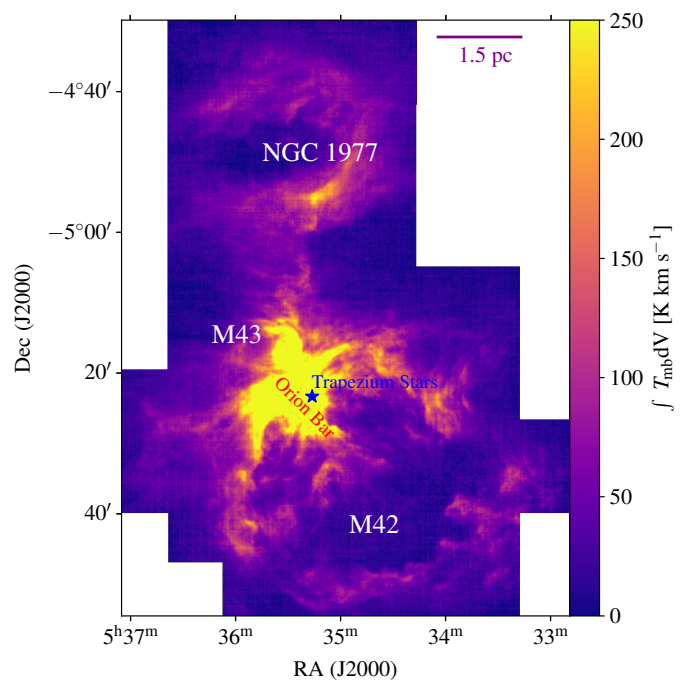


Fig. 1: [C II] $158 \mu\text{m}$ integrated line intensity map (from $v_{\text{LSR}} -50$ and $+50 \text{ km s}^{-1}$) of the OMC obtained with the upGREAT receiver onboard SOFIA. The bubbles of NGC 1977, M42, and M43 as well as the Trapezium stars and the Orion Bar are indicated. The 1.5 pc length is indicated by the line at the top-right.

idents on the Veil and to decompose the observed [C II] line profiles over the dent position. Section 4 contains an analysis of the momentum and energy of the dents. Finally, we discuss the origin of the dents and suggest possible further studies in Section 5.

2. Observations

2.1. [C II] observations

The observations were carried out with the Stratospheric Observatory for Infrared Astronomy (SOFIA), an airborne observatory project funded by the US National Aeronautics and Space Administration (NASA) and the German Aerospace Centre (DLR). SOFIA is a Boeing 747-SP jetliner that has been adapted to carry a 2.7-meter-diameter telescope in the back fuselage (Young et al. 2012).

The data were collected with the German REceiver for Astronomy at Terahertz Frequencies (upGREAT) Instrument onboard SOFIA (Risacher et al. 2018) for the Large program of the C^+ SQUAD led by A. G. G. M. Tielens. The spectral and spatial resolution during the observation is about 0.04 km s^{-1} , and $14.1''$. The final data were resampled to 0.3 km s^{-1} to achieve a better signal-to-noise ratio. The spatial resolution of the map is smoothed to $16''$, which corresponds to $\approx 0.03 \text{ pc}$ at the distance of Orion, 414 pc (Menten et al. 2007). The final rms noise (in T_{mb}) is 1.14 K in 0.3 km s^{-1} velocity channels. More information on the observations and data reduction can be found in Pabst et al. (2020); Higgins et al. (2021).

2.2. Molecular gas observations

We make use of $^{12}\text{CO } J=2-1$ (230.5 GHz) and $^{13}\text{CO } J=2-1$ (220.4 GHz) line maps taken with the IRAM 30m telescope in

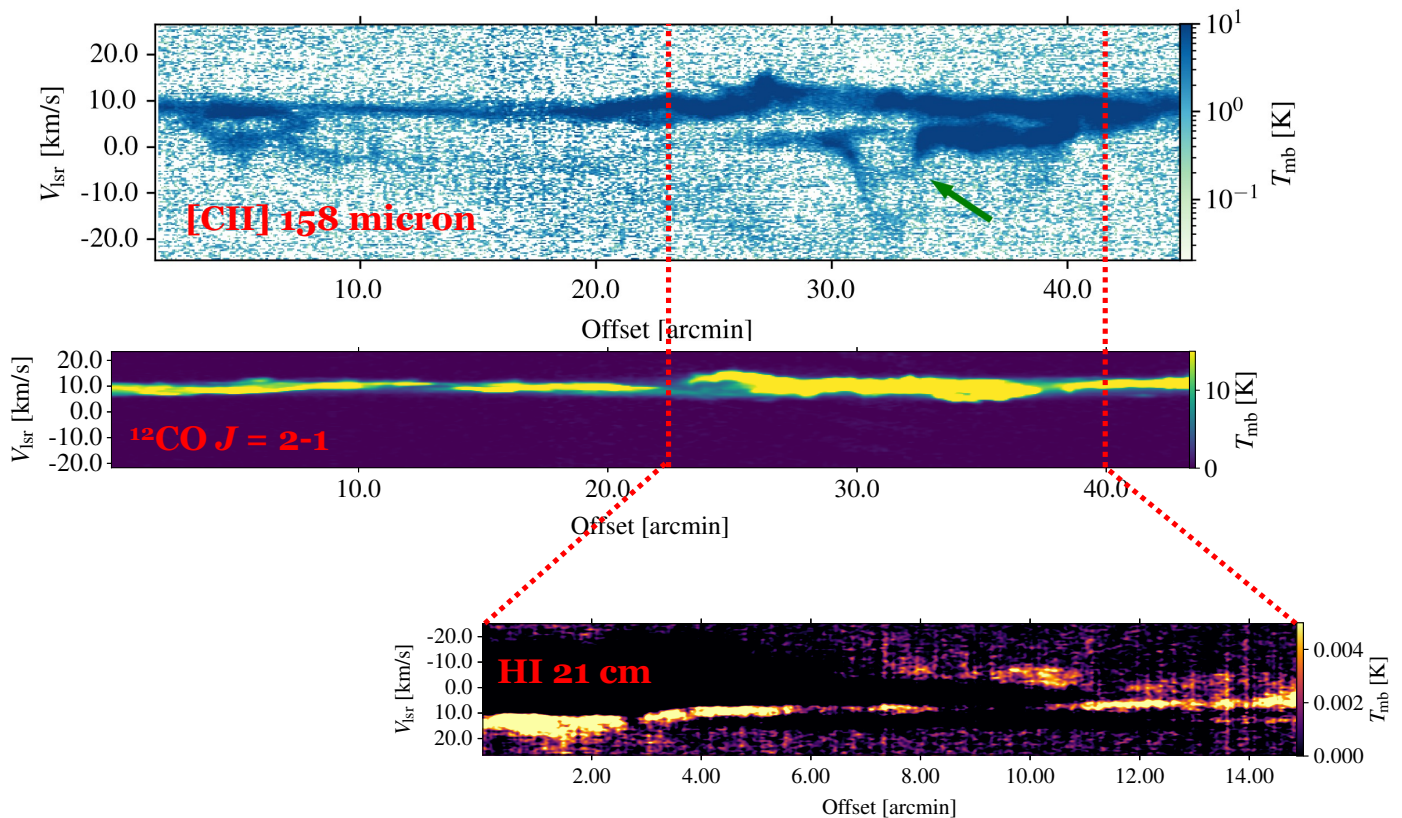


Fig. 2: PV diagrams of dent 4. The emission at a v_{LSR} velocity of $+9 \text{ km s}^{-1}$ is the OMC, the weak [C II] emission of Veil is at $v_{\text{LSR}} = -4 \text{ km s}^{-1}$. The dent at $33'$ is indicated by a green arrow in the [C II] $158 \mu\text{m}$ PV-diagram. The ^{12}CO and H I PV diagrams are shown in the middle and lower panels, respectively. H I observation from van der Werf et al. (2013) exist between the offset between two red-dashed lines, which $15'$ long, in the [C II] and CO observations. Dent 4 is located at $7.5'$ in the H I pv diagram.

the framework of the Large Program ‘Dynamic and Radiative Feedback of Massive Stars’ (PI: J. R. Goicoechea). In order to facilitate comparison with the velocity-resolved [C II] map, we smoothed the ^{12}CO (2-1) and ^{13}CO (2-1) data to the angular resolution of the SOFIA [C II] maps of $16''$. The average rms noise level in these maps is 0.16 K in 0.41 km s^{-1} velocity channels. A more detailed description of the CO observations can be found in Goicoechea et al. (2020).

2.3. Atomic gas observations

We use H I 21 cm observation of the Veil shell obtained with the Karl G. Jansky Very Large Array at C and K configurations. The observation has an angular resolution of $7.2'' \times 5.7''$ and a velocity resolution of 0.77 km s^{-1} . Further details on data reduction and observation can be found in van der Werf et al. (2013).

2.4. Mid-IR observations

Mid-infrared observations were taken with the space-borne Spitzer telescope (Werner et al. 2004) that conducted scientific observations between 2003 and 2020 with three focal plane instruments, one of which being the Infrared Array Camera (IRAC; Fazio et al. 2004). IRAC is a four-channel camera that produces 5.2×5.2 arcminute images at 3.6 , 4.5 , 5.8 , and $8 \mu\text{m}$. We utilize Spitzer $8 \mu\text{m}$ observations of the Orion Nebula to trace the UV-illuminated surface of the Veil. The FWHM of the point spread function is $1.9''$ at $8.0 \mu\text{m}$.

2.5. Far-IR photometric observations

The OMC has been observed as part of the Gould Belt Survey (André et al. 2010) in parallel mode using the Photoconductor Array Camera and Spectrometer ((PACS), Poglitsch et al. 2010) and Spectral and Photo-metric Imaging Receiver ((SPIRE), Griffin et al. 2010) instruments on-board *Herschel*. We use only the archival photometric images of PACS instrument at $70 \mu\text{m}$ tracing emission from warm dust grains for comparison with the [C II] map over the dents.

3. Identification of dents

The dents can be detected in velocity-resolved channel maps and position-velocity diagrams (Quillen et al. 2005). We first identify notable dents in [C II] PV diagrams along the Orion Veil (Section 3.1). We find that the dents emit at a v_{LSR} of -3 to -20 km s^{-1} , which is about -15 to -30 km s^{-1} blue-shifted from the OMC emission (Section 3.3). We then integrate the [C II] emission (green hue in Fig. 3) between these velocities to identify further dents in high-velocity [C II] channels (Section 3.2).

3.1. Position-velocity (PV) Diagrams

Because structures in the Veil are hard to find in the integrated map of [C II], the unbiased way of identifying shock-accelerated material or dents is the PV diagram. We examine [C II] PV diagrams of the Orion Veil produced with $30''$ broad horizontal and

vertical slices. The horizontal cuts (east-to-west) are 60' long, while the vertical cuts (south-to-north) are 45' long because of the non-spherical morphology of the Orion Nebula.

PV diagrams uncover the complicated structure of the Veil exposed to ionizing radiation from the Trapezium stars (O'Dell et al. 2017). In all PV diagrams, the [C II] emission at $v_{\text{LSR}} = +9 \text{ km s}^{-1}$ indicates the background cloud OMC-1 (see PV diagram of dent 4 in Fig. 2 and of all dents in Appendix C). The main blue-shifted expanding structure, moving towards us, is the Veil shell, expanding at 13 km s^{-1} (Pabst et al. 2019). In addition to these structures, we find ‘V-shaped’ substructures that expand faster than the Veil. Using [C II] PV diagrams, we identify four dents in the Veil, which are listed with their properties in Table 1. The expansion velocities are measured relative to the blue-shifted Veil shell. To this end, we extract the peak velocity, which is determined via Gaussian fitting of the dent spectrum, of the dent from that of the Veil component. The average size of the dents is about 0.3 pc, which is equal to $2.5'$. The size of the dent is calculated along the RA axis in the PV diagrams. Since we know the width of each crosscut, the size of the dent in Dec is estimated by the number of PV diagrams in which it appears.

Additionally, we examine the PV diagrams of the H I 21 cm and ^{12}CO observations of the Veil shell to see if the dent looks identical to that of [C II] 158 μm (see also Fig. 2). First of all, we find that van der Werf et al. (2013)'s H I observation covers four of the dents identified before in the [C II] PV diagrams. In Appendix C, we provide H I PV diagrams of these dents, respectively. Because the H I PV diagrams behave differently, the H I observations cannot be used to trace the dents.

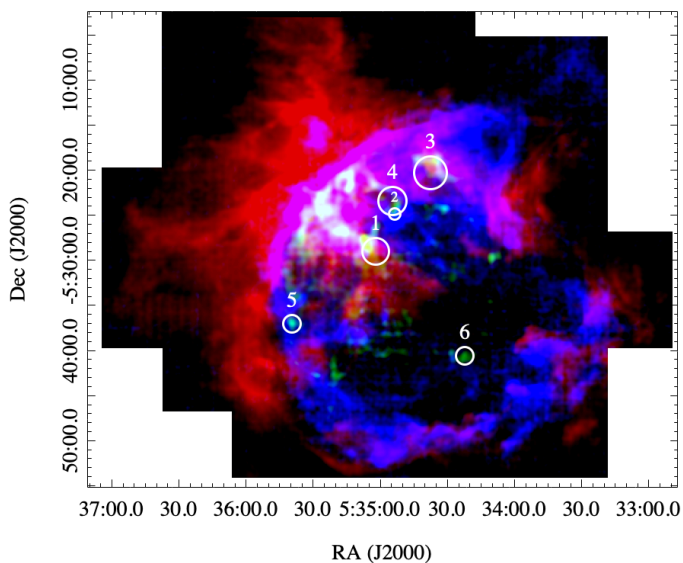


Fig. 3: Three-color map of [C II] emission in the Orion Nebula. Red hue represents the integrated [C II] emission from the OMC between $+20$ and $+3 \text{ km s}^{-1}$. Blue represents the blue-shifted [C II] emission generated by the Veil shell moving between $+3$ and -3 km s^{-1} . Green represents high-velocity [C II] emitting gas at velocities ranging from -3 to -20 km s^{-1} . Gaussian smoothing of radius $35''$ is performed to all three colors to reduce the image noise. The white circles indicate the position and size of the dents measured via PV diagrams that is also the aperture size for extracting [C II] line profiles of the dents. More information is given in Section 4.

3.2. High-velocity [C II] emission

As an alternative approach to identifying the interaction of stellar jets/outflows with the Veil, we peruse the [C II] channel maps. Inspection of these maps reveals [C II] emission between -20 and -3 km s^{-1} . We examine the [C II] channel maps, which show blue-shifted gas with a rather high velocity associated with the Veil. This is accomplished by superimposing the [C II] emission within this velocity range as a green hue across the [C II] of emission of the Veil (blue hue) and the OMC-1 background cloud (red hue) in Figure 3.

This procedure also results in identifying dents 1–4. In addition, two more locations of high-velocity [C II] emission become apparent (dents 5 and 6 in Fig. 3). These spots are the brightest and farthest high-velocity gases from the Trapezium cluster, respectively. The behaviour of these high-velocity structures does not appear as a dent in the PV diagrams (see Section 3.1). Examining the consecutive PV diagrams covering dents 5 and 6 shows that there is blue-shifted emission slightly faster than the Veil and that the velocity of the [C II] emitting gas increases towards the peak of these structures (see Figs. C.9 and C.10).

Note also that there is high-velocity [C II] emission we have not considered in this work, especially in the Huygens region. This region has been the subject of many publications: van der Werf et al. (2013); O'Dell (2001); O'Dell et al. (2009); Abel et al. (2019). The origin of this emission could be a combination of the radiative and mechanical feedback from the Trapezium cluster and perhaps also from the stars in the Orion-S cloud (O'Dell et al. 2009). We also note that we limit this work focusing on dent 5 and 6 detected in high-velocity [C II] emission, since other green hues, especially in Huygens region, exhibit very complex behavior and do not allow us to estimate the properties of the dents.

3.3. Line profiles

The [C II] emission towards the dents shows a complex structure in the PV diagrams. To explore the origin of each component, we extract the [C II] spectral line profiles across the six dents from the data cube and present them in Fig. 4 between LSR velocities of -30 and $+30 \text{ km s}^{-1}$. We utilize the size of the dent in arcminutes estimated from the PV diagrams to determine the size of the extraction region. In the direction of the dents, the line profile suggests a multi-component structure.

We used a multi-Gaussian model to fit the [C II] spectra and estimate the line parameters. The fit results are listed in Table A.1. In the local standard of rest, all [C II] spectra exhibit three major components: (i) the OMC at $+9 \text{ km s}^{-1}$, (ii) Orion's Veil at about -2 km s^{-1} , and (iii) the dents at -10 km s^{-1} . Dent 1 is an outlier, since it exhibits a double-peak at the Veil's velocity (i.e., black and orange fits) as well as a component at the extreme velocity of -19 km s^{-1} (see black Gaussian fit in Fig. 4).

Dents 5 and 6 behave slightly different than the other dents (Figs. C.9 and C.10). The PV diagrams of these dents appear to have a bright head of emission that is not linked with the Veil at first glance (see the PV diagram at the top in Figures C.9 and C.10). In addition, their brightness is similar to the Veil's. We check the spectra of the adjacent places to see if accelerated gas is present at the dent positions. According to the spectra in Fig. C.11, these two dents are expanding somewhat faster than the Veil. In Section 4, we provide information regarding the origin of the [C II] emission at the head of the dents.

Table 1: Dents identified in this work. The location and sizes of the dents are shown in Fig. 3.

ID	RA (J2000)	Dec (J2000)	$\int T_{\text{mb}} dv$ [K km s ⁻¹]	Size ^a (pc × pc)	$I_{\text{[C II]}}^b$		(f, α) ^c $d_{2.0 \text{ pc}}$	Mass [M_{\odot}]	$V_{\text{exp,dent}}$ [km s ⁻¹]	P_{dent} [M_{\odot} km s ⁻¹]
	(h:m:s)	(°:′:″)			(× Veil)	(× OMC)				
1	+05:35:01.5	-05:29:03.5	5.27 ± 1.51	0.36 × 0.24	0.65	0.04	5, 10	3.3 ± 0.6	6.40 ± 1.1	21.5 ± 1.3
2	+05:34:53.4	-05:24:56.7	9.91 ± 4.23	0.16 × 0.18	0.28	0.33	12, 5	0.6 ± 0.1	9.60 ± 3.4	6.00 ± 0.9
3	+05:34:37.4	-05:20:19.9	11.6 ± 3.18	0.43 × 0.30	0.62	0.11	5, 12	4.8 ± 0.9	8.00 ± 1.7	38.4 ± 3.2
4	+05:34:54.2	-05:23:30.5	6.27 ± 1.50	0.39 × 0.30	0.20	0.12	5, 11	3.9 ± 0.8	13.5 ± 1.7	52.5 ± 3.1
5	+05:35:39.2	-05:37:05.2	22.8 ± 1.25	0.12 × 0.12	1.35	1.00	16, 3	1.4 ± 0.3	9.20 ± 0.6	>13.6 ± 0.7
6	+05:34:22.0	-05:40:36.7	6.23 ± 3.61	0.24 × 0.24	0.92	0.46	16, 3	1.5 ± 0.3	4.30 ± 2.3	>6.40 ± 2.0

Notes. ^(a) One arcminute corresponds to the physical size of 0.12 pc at the distance of the Orion Nebula (414 pc; Menten et al. 2007). The error in size is around 10%. ^(b) $I_{\text{[C II]}}$ denotes the integrated intensities of the dent. The values indicate which component dominates [C II] emission at the dent position. If the value in the Veil and the OMC columns are > 1, that dent has brighter [C II] emission. For fit results, see Table A.1. ^(c) d , f , and α denote the distance between star and the Veil surface, the collimation factor and opening angle (in degree) of possible outflows, respectively. f and α are given for distances of 2.0 pc. See Section 4 for more detail.

4. Analysis

In Section 4.1, we summarize the properties of the dents. The momentum, which is the key parameter used to analyze the driving mechanism, of each dent is then estimated (Section 4.2) to comprehend the driving process. We compare the [C II] emission with two crucial PDR tracers in Section 4.3. Finally, we discuss a possible tracer of dent-like features on the ionization front of H II regions in Section 4.4.

4.1. Characteristics of the dents

In the previous section, we identify six dents that have diameters ranging from 0.16 to 0.43 pc. The first four dents in Table 1 stand out in PV diagrams, but the last two dents require confirmation by high-velocity [C II] emission maps. Four out of the six dents are detected near the Huygens region hosting the Trapezium cluster. The other two are in the direction of the extended Orion Nebula (EON; Güdel et al. 2008). None of the dents appear in ¹²CO-PV diagrams (see Appendix C) which suggest a low molecular gas fraction. Morphologically, all dents look like (shark) teeth in PV space and their v_{LSR} is more negative than that of the Veil shell. The expansion velocity of the dents relative to the Veil ranges from 4 to 14 km s⁻¹. Based on this, we suggest that the dents are made up of CO-dark H₂ gas similar to what is seen in the Orion Bar (van der Tak et al. 2012; Goicoechea et al. 2015; Kavak et al. 2019). The formation of H₂ remains unclear, but it could be reformed in the shocked gas.

4.2. Momentum of the dents

The momentum of the dent is estimated to determine the driving mechanism on the assumption that the momentum of outflows from protostars is conserved. In this regard, the mass and velocity of the dent must be estimated. We measure the expansion velocity relative to the Veil shell using the fit results of the [C II] line profiles. To this end, we subtract the velocity of the dent from that of the Veil (see Table A.1). The mass parameter is, however, rather uncertain because the Veil shell has density variations of up to a factor of ten and a low N_{H} of $\sim 10^{21}$ cm⁻² (Pabst et al. 2020) toward the line-of-sight. However, it is possible to make an estimation based on the mass calculation reported by Pabst et al. (2019).

The mass accelerated by shocks from the Veil shell outflow equals at least the mass entrained in each dent. As the size (2.7 pc) and gas mass (1500 M_{\odot}) of the Veil are known (Pabst et al. 2020), we can roughly calculate the surface mass density of

the Veil to calculate the mass parameter assuming a half-sphere geometry with radius of 2.7 pc for the Veil. The surface density of the Veil is $\sim 30 M_{\odot}$ pc⁻². We multiply the area of the dent with the surface density to estimate the shock-accelerated mass, in other words, the mass in the dents. The mass estimation and momentum of the dents are given in Table 1. We also note that Dents 5 and 6 are oblique to the surface of the Veil as shown by a series of PV-diagrams (see Figs. C.9 and C.10) in Appendix C. We, therefore, give a lower limit for the momentum of these two dents in Table 1.

The total momentum of the Veil is 18,000 M_{\odot} km s⁻¹ and the dents carry thus between 0.5 and 1% of the total momentum injected by the Trapezium stars (Pabst et al. 2020). For comparison, the momentum contained in the protrusion to the northwest is 540 M_{\odot} km s⁻¹ that is 3% of the momentum of the Veil shell (Kavak et al. 2022).

The correlation between the jet/outflow momentum and the luminosity of the protostars ejecting the material has been well established (Bontemps et al. 1996; Wu et al. 2004; López-Sepulcre et al. 2010; Duarte-Cabral et al. 2013; Sánchez-Monge et al. 2013; San José-García et al. 2013; Maud et al. 2015; Kavak et al. 2021). These results indicate a relationship across the low- and high-mass regimes between these two quantities (see Fig. 5). In this plot, each dent is individually marked by its momentum. The momentum of the dent implies massive stars of B-type with luminosities ranging between 10^3 and $10^4 L_{\odot}$. Also, because protostellar jets and outflows are typically double lobed, we double the momentum predicted for each dent in our sample before comparing it to the protostellar activity correlation.

Taking the size and the velocity as a guide, we estimate that the formation of the dents would take between $(0.5-2.5) \times 10^4$ years. This represents $\sim 1/4$ of the expansion timescale of the Veil shell ($\sim 2 \times 10^5$ years; Pabst et al. 2019), suggesting that the dents were produced during the expansion of the Veil by forming massive B- and A-type stars which is consistent with accreting massive stars reported by Duarte-Cabral et al. (2013). As this young age indicates recent outflow activity, we consider jets/outflows from accreting massive protostars as the most likely driving mechanism.

4.3. Origin of the dents

We look for correlations between the dent [C II] emission and tracers of UV versus shock illumination. For this, we make use of [C II] emission with PDR tracers such as Spitzer 8 μm PAH emission and PACS 70 μm tracing warm dust (see Fig. 6).

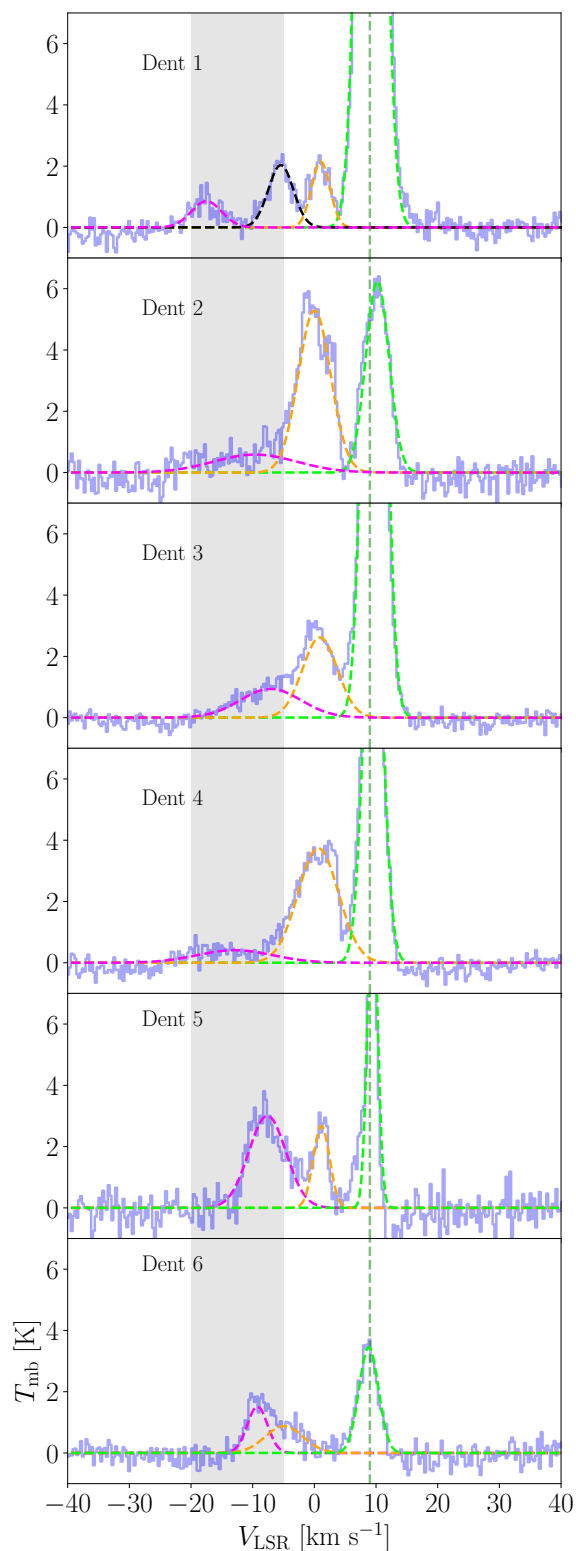


Fig. 4: [C II] 158 μm line profiles using a circular extraction aperture of dent-size width towards the Veil dents listed in Table 1. The vertical green-dashed lines indicate the system velocity (+9 km s^{-1}) of Orion. The light-green Gaussian fitting line is the OMC, the orange fitting line is the Veil, and the magenta fitting line is the dent. The black is component observed at the v_{LSR} of -5 km s^{-1} is a velocity component seen at the south of the Orion Bar PDR in the Huygens region.

Dent 1 is located just south-west the bright Orion Bar PDR. The spectrum in the direction of the dent has four components (see Fig. 4). The fitted lines in magenta, orange, and green represent the dent, the Veil shell, and background cloud OMC, respectively. The black component is observed at a v_{LSR} of -5 km s^{-1} . This component has been interpreted as a broad arc in the shape of an incomplete semicircle near the border of the Huygens region, but the dent at -18 km s^{-1} is not seen in H I 21 cm observations (van der Werf et al. 2013). The semicircle structure host a group of stars including a B-star (see Fig. B.1). We suggest that dent 1 is accelerated by the jet/outflow of these stars to an v_{LSR} velocity of $+20 \text{ km s}^{-1}$. We also suggest that these dents reflect the interaction of jets/outflows with the expanding Veil nebula. The velocity of these jets/outflows must be in excess of the expansion velocity (13 km/s; Pabst et al. 2019) of the Veil itself. We will come back to this hypothesis in Section 5.

Luhman et al. (1994) concluded that UV fluorescence dominates the extended IR H_2 ($v>0$) emission toward OMC. Indeed, the extended K_s emission (including the H_2 $v=1-0$ S(1) and $v=2-1$ S(1) lines) spatially correlates with the CH^+ $J=1-0$ emission (Goicoechea et al. 2019), a natural product of reactions between C^+ and UV-pumped H_2 ($v>0$) (e.g., Agúndez et al. 2010). The extended Orion Nebula has been surveyed in the 1-0 S(1) line at $2.12 \mu\text{m}$ by (Stanke et al. 2002). We find that 12 out of 78 H_2 features are situated in the direction of the Orion Nebula but are unconnected to the dents because the structures reported by Stanke et al. (2002) are found in dense molecular clouds while dents are associated with the diffuse emission in the Orion Veil. We conclude that shocks revealing the interaction of protostellar jets with the Veil nebula are difficult to trace directly. The best signature seems to be the velocity shift and broader line-widths induced by this shock interaction in the atomic fine-structure cooling lines but, as argued above, the [C II] emission is dominated by UV heated gas (see Section 4.4).

4.4. Potential shock signature of the dents

If the dents are indeed due to a jet interacting with the Veil, then we would expect to see this region light up in typical shock tracers. Low velocity interstellar shocks can be J-type or C-shocks, depending on the strength of the magnetic field and the shock velocity (Draine et al. 1983). The line-of-sight magnetic field is measured to be $\sim 100 \mu\text{G}$ (Troland et al. 2016). For atomic gas, the critical velocity at which a C-shock becomes J-type is $\sim 20 \text{ km s}^{-1}$ (Lesaffre et al. 2013). The observed velocities are consistent with a C-type shock in the range of 5 to 15 km s^{-1} . Such a shock would heat a column density of $\sim 10^{20} \text{ cm}^{-2}$ to $\sim 1000 \text{ K}$ (Lesaffre et al. 2013). For a velocity in excess of 20 km s^{-1} , the shock would be J-type. The gas is then heated to $\sim 10^5 \text{ K}$ in the shock front and, in the frame of the shock, would flow at 1/4 of the shock velocity. As the gas cools down, its velocity would decrease. In a J-type shock, cooling through atomic lines becomes more important.

Comparing PDR models (Kaufman et al. 2006; Pound & Wolfire 2008) and shock models, for the atomic cooling lines ([C II], [O I], [C I], and etc.), the shock signature would be overwhelmed by the emission generated by the UV irradiation. The best tracers are low- J H_2 lines (Lesaffre et al. 2013) but there too, the UV-heated gas would have to be accounted for. As an example, the H_2 0-0 S(1) intensity from a PDR with $G_0 = 10^2$ is predicted to be $10^{-5} \text{ erg cm}^{-2} \text{ s}^{-1} \text{ sr}^{-1}$; very comparable to the emission from a 10 km s^{-1} C-type shock and about 10 times the emission from a J-type shock (Lesaffre et al. 2013). High-velocity J-type shocks will lead to emission in optical transitions

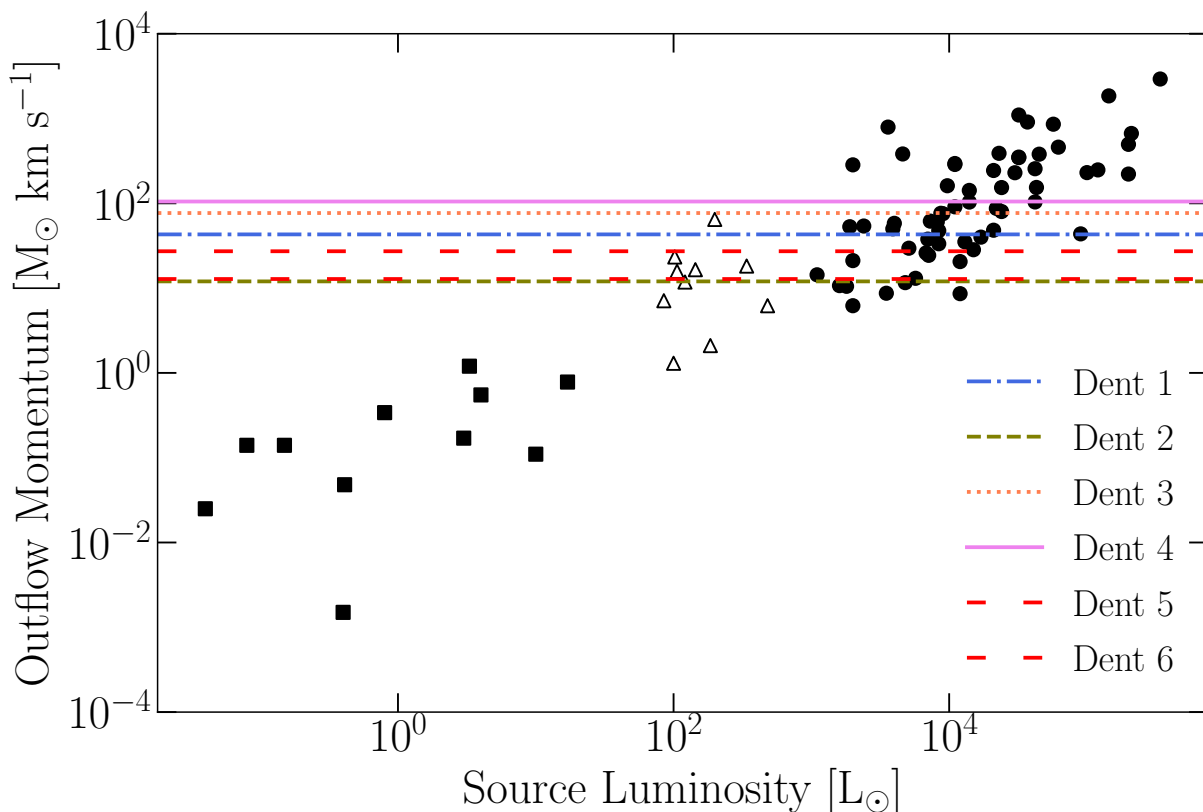


Fig. 5: Plot of outflow momentum in $M_{\odot} \text{ km s}^{-1}$ against the luminosity of its driving source in L_{\odot} . Black circles are from [Maud et al. \(2015\)](#), and open triangles from [Duarte-Cabral et al. \(2013\)](#) for high-mass Class-0 objects, and black squares from [Dunham et al. \(2014\)](#) showing the outflows from low-mass stars. Horizontal lines denote the momentum (multiplied by two as outflows are bipolar) of each dent listed in Table 1. Dent 5 and 6 have a lower limit, and thus are indicated by red loosely-dashed lines.

such as [S II] $\lambda 6731$. High velocity resolution will be required to separate this shock emission from photo-ionized gas in the extended Orion Nebula. Finally, we note that the substantial column density of warm gas in both C- and J-type shocks would enable reactions with substantial energy barriers to proceed and this could lead to detectable amounts of, for example, OH, and SH^+ ([Lesaffre et al. 2013](#); [Godard et al. 2019](#)). As shocks heat the gas to much higher temperatures than PDRs, these species could be used as the signature of the presence of a shock. Similarly, high-spectral resolution observations of near-IR [Fe II] and IR [S I] and [Ne II] lines could be used as shock tracers because these lines originate from levels that cannot be excited in low density, low UV field PDRs.

In the dents, the [C II] $158 \mu\text{m}$ line-widths are always broader than those from the background OMC-1 cloud (see Table A.1). Also, with the exception of Dents 5 and 6, the line-widths of the dent components are broader than that of the Veil, although the fit uncertainty is sometimes large. There could be a few possibilities to explain the broad line-widths: (a) the gas in the dents is warmer than the gas in the Veil, (b) or it is much more turbulent, as a result of the passage of the shock, (c) lines are broad because the [C II] emission is from hot photoionised gas rather than neutral gas. The observed line width (σ) in the dents is,

$$\sigma = (\sigma_{\text{th}}^2 + \sigma_{\text{turb}}^2)^{1/2} \quad (1)$$

where σ_{turb} is the non-thermal velocity dispersion and σ_{th} is thermal broadening which change as $(kT_k/m_{\text{C}^+})^{1/2}$. This analysis is applicable to optically thin [C II] emission, i.e., with no opacity broadening. First, we assume that $\sigma_{\text{turb}} = 0$. For the observed

line-widths (with median value of 9.36 km s^{-1} in Table A.1), we require a maximum temperature (T_k) of the gas of $5 \times 10^4 \text{ K}$, which is significantly higher than than the neutral gas in Orion molecular cloud ([Goicoechea et al. 2015](#)). This may imply that [C II] emission arises from a more turbulent gas in the Veil shell. To compute σ_{turb} , we also assume that the [C II] gas in the dents is at $T_k \sim 100 \text{ K}$ ([Pabst et al. 2020](#)). At $T_k \sim 100 \text{ K}$, the speed of sound is $\sim 1 \text{ km s}^{-1}$, and σ_{turb} is 9 km s^{-1} for the line width of 9.36 km s^{-1} given in Table A.1. This gives us non-thermal velocity distribution (σ_{turb}), which is $\Delta v_{\text{FWHM}}/2.355$, of $\sim 4 \text{ km s}^{-1}$. This is greater than the speed of sound at 100 K indicating that nonthermal velocity distribution in the dents is as a result of turbulent motions such as shocked gas within jets/outflows.

4.5. Collimation factor and opening angle

Assuming that the dents are driven by the jets/outflows of protostars, the collimation factor (f) may also be an indication of the type of star given that outflow collimation decreases from low to massive stars ([Bachiller & Tafalla 1999](#)). However, outflows from B- or O-type stars can be well-collimated with factors higher than five on a dynamical timescale shorter than 10^4 yr ([Arce et al. 2007](#)). Moreover, [Wu et al. \(2004\)](#) report that the collimation factor of the outflow from a protostar with bolometric luminosity higher than $10^3 L_{\odot}$ is about two. In our case, the degree of collimation can be estimated depending on the distance (d) between the star and the surface of the Veil shell (see also Fig. B.1 for the assumed geometry). For this purpose, we assume that the star, which is powering the outflow is located in the core

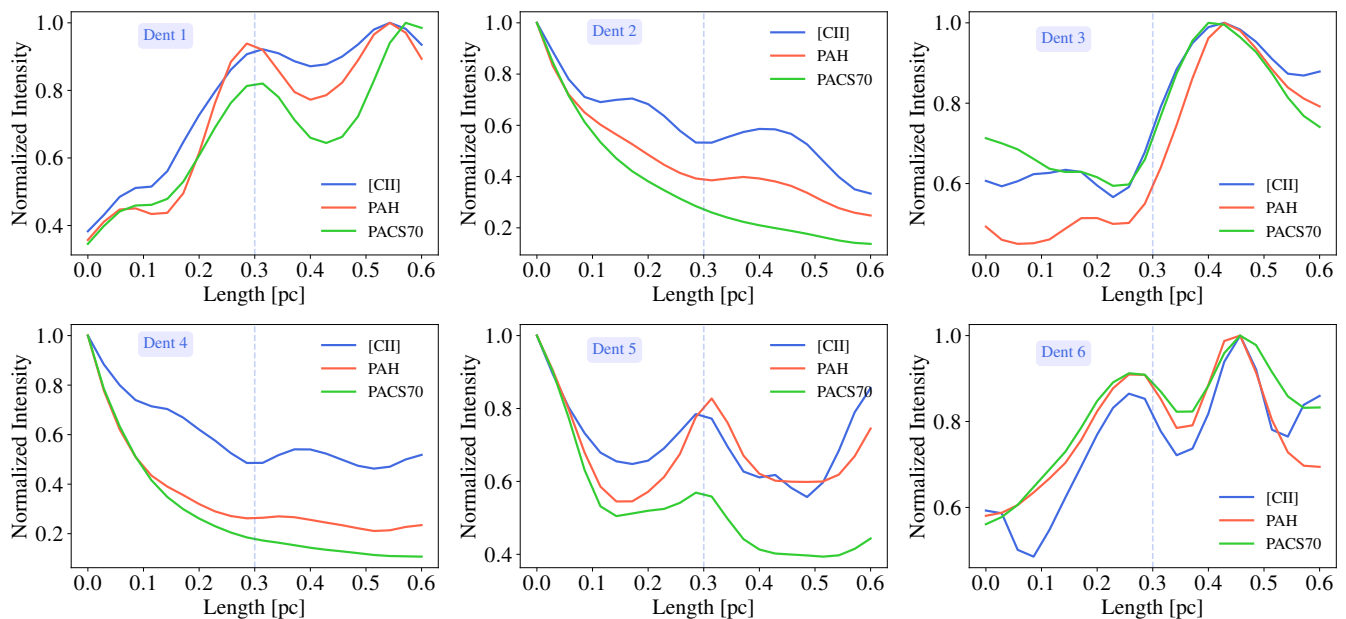


Fig. 6: Comparison of normalized [C II] intensity with to that of 8 μm and PACS 70 μm along 0.6 pc long horizontal cuts spanning the dents from east-to-west. The position of the dent is shown by the vertical blue-dashed line. All observations are convolved to 20'' for a proper comparison.

of the Orion Nebula cluster at a distance of 2 pc. The collimation factor varies between 5 and 12 while the opening angle (α) is between 3 and 12° (see Table 1), indicating collimated ejections such as molecular jets from massive stars (Arce et al. 2007). If the star-dent distance were substantially smaller than the adopted value, the collimation factor would decrease and the opening angle would increase. For a distance of 0.5 pc, the typical collimation factor and opening angle would be 2 and 40°, respectively. We estimate a timescale of 5.5×10^4 years (see timescale above) for dent 1 involved in its formation, which is 1/4 of the expansion timescale of the Veil shell (Pabst et al. 2019). With this kind of a timescale, the star does not need to be directly behind the dent because a massive star with a proper motion of 2 km s⁻¹ can travel about 0.1 pc ($\sim 0.8'$) away in 5.5×10^4 years from where its outflows were ejected. Therefore, estimating the driving stars of the dents is challenging.

In addition, the [C II] spectra around dents 5 and 6 suggest [C II] emission from accelerated gas (see Fig. C.11). Only these two dents show an increase in [C II] brightness at the head of the dents. By comparing the intensities in Fig. 6 and previous findings in Section 3, we argue that these two dents are also formed by the same mechanisms on the surface of the Veil shell. We, however, are unable to find the same association for all dents in Fig. 6 (see also Table 1) because the [C II] emission of the Veil and the OMC dominate the [C II] emission of Dents 1–4.

5. Summary

Using SOFIA [C II] observations, we trace the influence of protostellar feedback by protostars on the Orion Veil. To that aim, we employ PV diagrams and maps of blue-shifted [C II] emission ranging from $v_{\text{LSR}} = -3$ to -20 km s⁻¹. A dent is defined as a shock-accelerated structure that expands outward on the Veil shell. We identify six dents in the Veil shell that are expanding towards us. Their sizes vary between 0.16 and 0.43 pc and they expand at velocities from 4 to 14 km s⁻¹. Kavak et al. (2022) found that fossil outflows, generated by the Trapezium stars dur-

ing their protostellar phase, influence the shape of the Veil shell as well. The momentum of the dents indicates newly forming stars with luminosities between 10^3 and $10^4 L_{\odot}$, i.e., B-type stars. The dents are, therefore, a consequence of the collision of active, energetic jets/outflows expelled by massive protostars with the surrounding swept-up shell. The Veil shell is being driven mainly by the stellar wind of θ^1 Ori C, the most dominant star in the Trapezium cluster (Abel et al. 2019; Pabst et al. 2019). The Trapezium stars are on the main sequence and this wind is the result of radiation pressure acting on gas in the stellar photosphere. In contrast, the jets and outflows considered for the dents are driven by accretion onto a protostar. We conclude that, in addition to radiative feedback, both active and fossil outflow processes have a significant impact on the morphology of the Veil shell.

The total momentum in the dents are $\sim 1\%$ of the momentum carried by the Veil shell. Kavak et al. (2022) identified approximately twenty B-type stars in the direction of the Orion Nebula. Half of the twenty stars appear to be located within the Orion Nebula. We discovered six dents in all, and may missed four of them. These, we believe, could be located in the direction of the Huygens regions, which have a complex morphology. We also speculate that these protostellar jets and outflows may create channels and holes in the Veil that might allow the 10^6 K plasma to escape the Veil confinement. Any escaping hot plasma will entrain further Veil material and widen the dent aperture. Eventually, the escape of the hot plasma will relieve the pressure of the wind-blown bubble. At that point, the expansion of the Veil will enter a momentum conserving phase and eventually merge with the material in the Orion-Eridanus superbubble. Supernova explosions in the Orion Ia/Ib associations will sweep up this loose material and transport it to the walls of this superbubble (Ochsendorf et al. 2015). Further evidence is required to support this hypothesis.

According to van der Werf et al. (2013); Abel et al. (2019), the Veil shell is ionized by the Trapezium stars and has a multilayered structure along the line-of-sight. Because shocks in

jets/outflows with high velocities in low-density slabs (see also Lehmann et al. 2020) interact with the Veil, they may cause extra [C II] emission on the Veil surface. This might be attributed to a variety of factors. To begin with, the Veil shell has a low, varying N_{H} toward the line-of-sight as it shows also a density gradient, which might suggest that there is insufficient material on the Veil surface to excite. In addition, the dents are positioned in front of the background OMC-1 cloud, which is likewise exposed to intense UV-radiation of Trapezium stars. This radiation may dominate additional [C II] emission produced as a result of shock-cloud interaction.

Without velocity-resolved [C II] observations, it is challenging to unveil the dent-like structure on the Veil shell. Estimating the driving stars of the dents is also difficult as that star could have moved from the ejection point of its jets/outflows. Unlike CO-globules found in the Veil shell (Goicoechea et al. 2020), the dents do not show up in ^{12}CO -PV diagrams. This shows that, like the Veil itself, their N_{H} is low because the dents are accelerated from the Veil.

In the future, we plan to search for alternative tracers to follow the dents of the Veil and validate the presence of jets/outflows at their location. For this purpose, long-slit spectra of $1.644\ \mu\text{m}$ [Fe II] line, and [S II] as can for example be observed with the ARCTIC instrument employed at Apache Point Observatory with high-resolution ($>10,000$) might aid in determining the dynamics of the dents. Finally, we conclude that velocity-resolved [C II] observations of SOFIA observatory continue to be state-of-the-art for discovering feedback mechanisms in massive star forming regions.

6. Discussion

The Orion Nebula is the closest massive star-forming region, providing an excellent opportunity to study fundamental stellar feedback mechanisms. Recently SOFIA observations revealed that the Orion Veil shell is primarily driven by the stellar winds of θ^1 Ori C, an O6 type star in main-sequence-phase, and that the northern half of the Veil shell was damaged by its now-extinct outflows. While a single massive star that is θ^1 Ori C mainly dominates the most energetic mechanisms in Orion, other regions may include a varying number of massive stars as well as newly formed stars of different masses. Other massive star-forming regions are located further away from Orion, posing problems with spatial resolution and velocity components along the line-of-sight. The size of the dents varies by approximately 0.3 pc, and this type of structure may be resolved in Doppler space in a region five times the distance from the Orion Nebula. We will use velocity-resolved [C II] line observation to search for dent-like structures in massive star forming regions to see if they are common in star-forming regions. In this context, the SOFIA FEEDBACK Legacy program (Schneider et al. 2020) will provide [C II] line observations of eleven massive star-forming regions at $158\ \mu\text{m}$.

Acknowledgements. We thank Antoine Gusdorf for useful discussions on the shock models and Paul van der Werf for providing H I 21 cm observation of the Orion Veil. Studies of interstellar dust and gas at Leiden Observatory are supported by a Spinoza award from the Dutch Science agency, NWO. JRG thanks the Spanish MICINN for funding support under grant PID2019-106110GB-I00. This study was based on observations made with the NASA/DLR Stratospheric Observatory for Infrared Astronomy (SOFIA). SOFIA is jointly operated by the Universities Space Research Association Inc. (USRA), under NASA contract NAS2-97001, and the Deutsches SOFIA Institut (DSI), under DLR contract 50 OK 0901 to the University of Stuttgart. upGREAT is a development by the MPI für Radioastronomie and the KOSMA/Universität zu Köln, in cooperation with the DLR Institut für Optische Sensorsysteme. We acknowledge the work, during the C+ upGREAT square degree survey of Orion, of the USRA and NASA staff

of the Armstrong Flight Research Center in Palmdale, the Ames Research Center in Mountain View (California), and the Deutsches SOFIA Institut.

References

- Abel, N. P., Ferland, G. J., & O'Dell, C. R. 2019, *ApJ*, 881, 130
 Abel, N. P., Ferland, G. J., O'Dell, C. R., & Troland, T. H. 2016, *ApJ*, 819, 136
 Agúndez, M., Goicoechea, J. R., Cernicharo, J., Faure, A., & Roueff, E. 2010, *ApJ*, 713, 662
 André, P., Men'shchikov, A., Bontemps, S., et al. 2010, *A&A*, 518, L102
 Arce, H. G., Shepherd, D., Gueth, F., et al. 2007, in *Protostars and Planets V*, ed. B. Reipurth, D. Jewitt, & K. Keil, 245
 Bachiller, R. & Tafalla, M. 1999, in *NATO Advanced Study Institute (ASI) Series C*, Vol. 540, *The Origin of Stars and Planetary Systems*, ed. C. J. Lada & N. D. Kylafis, 227
 Bally, J. 2016, *ARA&A*, 54, 491
 Bally, J., Licht, D., Smith, N., & Walawender, J. 2006, *AJ*, 131, 473
 Beuther, H., Schilke, P., Sridharan, T. K., et al. 2002, *A&A*, 383, 892
 Bontemps, S., André, P., Terebey, S., & Cabrit, S. 1996, *A&A*, 311, 858
 Draine, B. T., Roberge, W. G., & Dalgarno, A. 1983, *ApJ*, 264, 485
 Duarte-Cabral, A., Bontemps, S., Motte, F., et al. 2013, *A&A*, 558, A125
 Dunham, M. M., Arce, H. G., Mardones, D., et al. 2014, *ApJ*, 783, 29
 Fazio, G. G., Hora, J. L., Allen, L. E., et al. 2004, *ApJS*, 154, 10
 Godard, B., Pineau des Forêts, G., Lesaffre, P., et al. 2019, *A&A*, 622, A100
 Goicoechea, J. R., Pabst, C. H. M., Kabanovic, S., et al. 2020, *A&A*, 639, A1
 Goicoechea, J. R., Santa-Maria, M. G., Bron, E., et al. 2019, *A&A*, 622, A91
 Goicoechea, J. R., Teyssier, D., Etxaluzte, M., et al. 2015, *ApJ*, 812, 75
 Griffin, M. J., Abergel, A., Abreu, A., et al. 2010, *A&A*, 518, L3
 Grudić, M. Y., Guszejnov, D., Hopkins, P. F., Offner, S. S. R., & Faucher-Giguère, C.-A. 2021, *MNRAS*, 506, 2199
 Güdel, M., Briggs, K. R., Montmerle, T., et al. 2008, *Science*, 319, 309
 Guszejnov, D., Grudić, M. Y., Hopkins, P. F., Offner, S. S. R., & Faucher-Giguère, C.-A. 2021, *MNRAS*, 502, 3646
 Haid, S., Walch, S., Seifried, D., et al. 2018, *MNRAS*, 478, 4799
 Henney, W. J., O'Dell, C. R., Zapata, L. A., et al. 2007, *AJ*, 133, 2192
 Higgins, R., Kabanovic, S., Pabst, C., et al. 2021, *A&A*, 652, A77
 Kaufman, M. J., Wolfire, M. G., & Hollenbach, D. J. 2006, *ApJ*, 644, 283
 Kavak, Ü., Goicoechea, J. R., Pabst, C. H. M., et al. 2022, *arXiv e-prints*, arXiv:2202.04711
 Kavak, Ü., Sánchez-Monge, Á., López-Sepulcre, A., et al. 2021, *A&A*, 645, A29
 Kavak, Ü., van der Tak, F. F. S., Tielens, A. G. G. M., & Shipman, R. F. 2019, *A&A*, 631, A117
 Krumholz, M. R., Bate, M. R., Arce, H. G., et al. 2014, in *Protostars and Planets VI*, ed. H. Beuther, R. S. Klessen, C. P. Dullemond, & T. Henning, 243
 Lehmann, A., Godard, B., Pineau des Forêts, G., & Falgarone, E. 2020, *A&A*, 643, A101
 Lesaffre, P., Pineau des Forêts, G., Godard, B., et al. 2013, *A&A*, 550, A106
 Lopez, L. A., Krumholz, M. R., Bolatto, A. D., Prochaska, J. X., & Ramirez-Ruiz, E. 2011, *ApJ*, 731, 91
 López-Sepulcre, A., Cesaroni, R., & Walmsley, C. M. 2010, *A&A*, 517, A66
 Luhman, M. L., Jaffe, D. T., Keller, L. D., & Pak, S. 1994, *ApJ*, 436, L185
 Luisi, M., Anderson, L. D., Schneider, N., et al. 2021, *Science Advances*, 7, eabe9511
 Maud, L. T., Moore, T. J. T., Lumsden, S. L., et al. 2015, *MNRAS*, 453, 645
 Menten, K. M., Reid, M. J., Forbrich, J., & Brunthaler, A. 2007, *A&A*, 474, 515
 Motte, F., Bontemps, S., & Louvet, F. 2018, *ARA&A*, 56, 41
 Ochsendorf, B. B., Brown, A. G. A., Bally, J., & Tielens, A. G. G. M. 2015, *ApJ*, 808, 111
 O'Dell, C. R. 2001, *ARA&A*, 39, 99
 O'Dell, C. R. 2018, *MNRAS*, 478, 1017
 O'Dell, C. R., Ferland, G. J., Henney, W. J., et al. 2015, *AJ*, 150, 108
 O'Dell, C. R., Ferland, G. J., Porter, R. L., & van Hoof, P. A. M. 2011, *ApJ*, 733, 9
 O'Dell, C. R., Hartigan, P., Bally, J., & Morse, J. A. 1997, *AJ*, 114, 2016
 O'Dell, C. R., Henney, W. J., Abel, N. P., Ferland, G. J., & Arthur, S. J. 2009, *AJ*, 137, 367
 O'Dell, C. R., Kollatschny, W., & Ferland, G. J. 2017, *ApJ*, 837, 151
 Olivier, G. M., Lopez, L. A., Rosen, A. L., et al. 2021, *ApJ*, 908, 68
 Pabst, C., Higgins, R., Goicoechea, J. R., et al. 2019, *Nature*, 565, 618
 Pabst, C. H. M., Goicoechea, J. R., Teyssier, D., et al. 2020, *A&A*, 639, A2
 Peimbert, M., Sarmiento, A., & Fierro, J. 1991, *PASP*, 103, 815
 Poglitsch, A., Waelkens, C., Geis, N., et al. 2010, *A&A*, 518, L2
 Pound, M. W. & Wolfire, M. G. 2008, in *Astronomical Society of the Pacific Conference Series*, Vol. 394, *Astronomical Data Analysis Software and Systems XVII*, ed. R. W. Argyle, P. S. Bunclark, & J. R. Lewis, 654
 Quillen, A. C., Thorndike, S. L., Cunningham, A., et al. 2005, *ApJ*, 632, 941
 Risacher, C., Güsten, R., Stutzki, J., et al. 2018, *Journal of Astronomical Instrumentation*, 7, 1840014

- San José-García, I., Mottram, J. C., Kristensen, L. E., et al. 2013, *A&A*, 553, A125
- Sánchez-Monge, Á., López-Sepulcre, A., Cesaroni, R., et al. 2013, *A&A*, 557, A94
- Schneider, N., Simon, R., Guevara, C., et al. 2020, *PASP*, 132, 104301
- Seo, Y. M., Goldsmith, P. F., Walker, C. K., et al. 2019, *ApJ*, 878, 120
- Stanke, T., McCaughrean, M. J., & Zinnecker, H. 2002, *A&A*, 392, 239
- Tan, J. C., Beltrán, M. T., Caselli, P., et al. 2014, in *Protostars and Planets VI*, ed. H. Beuther, R. S. Klessen, C. P. Dullemond, & T. Henning, 149
- Thielemann, F. K., Hirschi, R., Liebendörfer, M., & Diehl, R. 2011, *Massive Stars and Their Supernovae*, ed. R. Diehl, D. H. Hartmann, & N. Prantzos, Vol. 812, 153–232
- Tiwari, M., Karim, R., Pound, M. W., et al. 2021, *ApJ*, 914, 117
- Troland, T. H., Goss, W. M., Brogan, C. L., Crutcher, R. M., & Roberts, D. A. 2016, *ApJ*, 825, 2
- van der Tak, F. F. S., Ossenkopf, V., Nagy, Z., et al. 2012, *A&A*, 537, L10
- van der Werf, P. P., Goss, W. M., & O’Dell, C. R. 2013, *ApJ*, 762, 101
- Walch, S. K., Whitworth, A. P., Bisbas, T., Wünsch, R., & Hubber, D. 2012, *MNRAS*, 427, 625
- Werner, M. W., Roellig, T. L., Low, F. J., et al. 2004, *ApJS*, 154, 1
- Wu, Y., Wei, Y., Zhao, M., et al. 2004, *A&A*, 426, 503
- Young, E. T., Becklin, E. E., Marcum, P. M., et al. 2012, *ApJ*, 749, L17
- Zinnecker, H. & Yorke, H. W. 2007, *ARA&A*, 45, 481

Appendix A: Gaussian Fitting Results

Table A.1: Fit results of multi-Gaussian fitting to [C II] line profiles in Fig. 4.

Component	Position	v_{LSR} [km s ⁻¹]	$\int T_{\text{mb}} \delta V$ [K km s ⁻¹]	ΔV [km s ⁻¹]	T_{mb} [K]
Dent	1	-17.5 ± 0.81	5.27 ± 1.51	5.77 ± 1.92	0.85 ± 0.25
	2	-9.59 ± 3.34	9.91 ± 4.23	15.8 ± 6.46	0.58 ± 0.09
	3	-7.09 ± 1.55	11.6 ± 3.18	11.6 ± 2.54	0.94 ± 0.09
	4	-12.8 ± 1.63	6.27 ± 1.50	14.3 ± 4.01	0.41 ± 0.06
	5	-7.62 ± 0.19	22.8 ± 1.25	7.12 ± 0.47	3.00 ± 0.16
	6	-9.23 ± 0.29	6.23 ± 3.61	3.86 ± 0.84	1.51 ± 0.58
Veil	1	$+1.02 \pm 0.27$	8.02 ± 1.36	3.50 ± 0.68	2.15 ± 0.31
	2	$+0.01 \pm 0.10$	34.7 ± 3.52	6.16 ± 0.33	5.29 ± 0.32
	3	$+0.90 \pm 0.21$	18.6 ± 3.07	6.67 ± 0.49	2.62 ± 0.28
	4	$+0.63 \pm 0.12$	30.9 ± 1.37	7.76 ± 0.31	3.74 ± 0.09
	5	$+0.92 \pm 0.48$	16.8 ± 2.06	9.96 ± 1.46	1.59 ± 0.10
	6	-4.91 ± 1.98	6.74 ± 3.82	7.23 ± 2.91	0.87 ± 0.18
OMC	1	$+9.21 \pm 0.02$	146.7 ± 1.3	4.18 ± 0.04	32.9 ± 0.29
	2	$+10.2 \pm 0.06$	29.43 ± 0.8	4.42 ± 0.01	6.24 ± 0.16
	3	$+9.76 \pm 0.01$	106.5 ± 0.44	3.70 ± 0.02	27.0 ± 0.10
	4	$+9.54 \pm 0.02$	51.0 ± 0.55	3.62 ± 0.04	13.2 ± 0.12
	5	$+9.33 \pm 0.02$	23.0 ± 0.58	1.87 ± 0.04	11.5 ± 0.22
	6	$+8.81 \pm 0.61$	13.6 ± 0.46	3.71 ± 0.14	3.45 ± 0.11

Appendix B: Massive Stars and Geometry

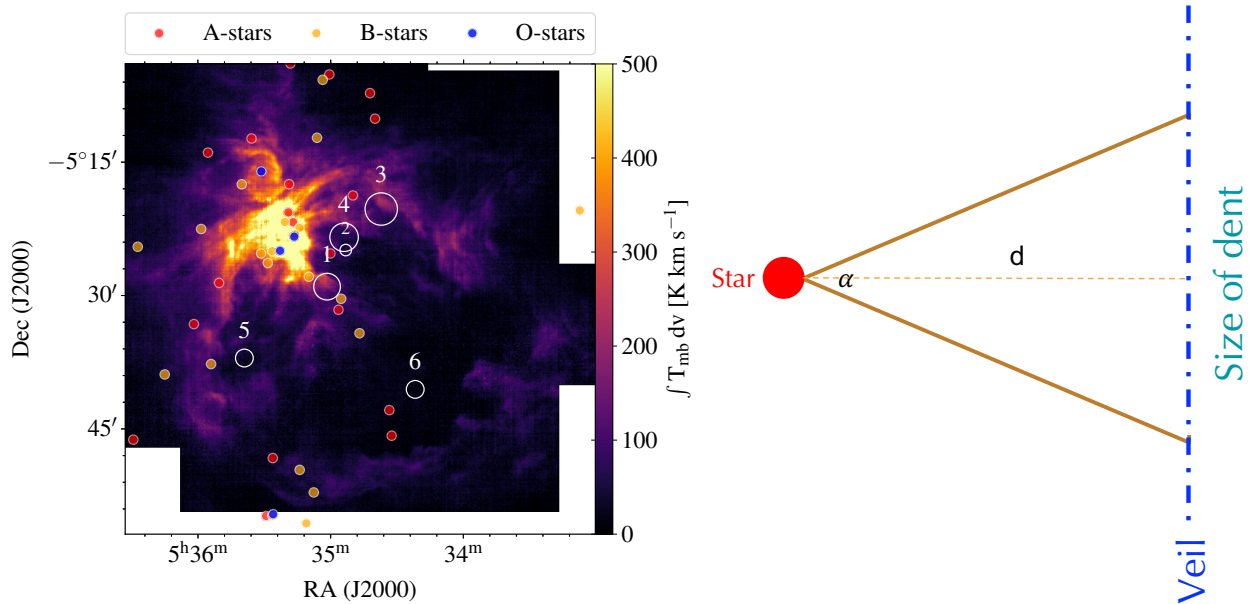


Fig. B.1: *Left*: SOFIA [C II] map of Orion with O-, B-, and A-stars found in SIMBAD. The blue-, orange-, and red-filled circles are O-, B-, and A-stars, respectively. White open circles indicate the dents identified in this work. *Right*: Geometry we used to calculate the collimation factor and opening angle (α).

Appendix C: PV diagram of the dents

This section contains a series of PV diagrams that cover the dents studied in this work. The length of all PV diagrams is 60'. Dents are indicated by a colored arrow.

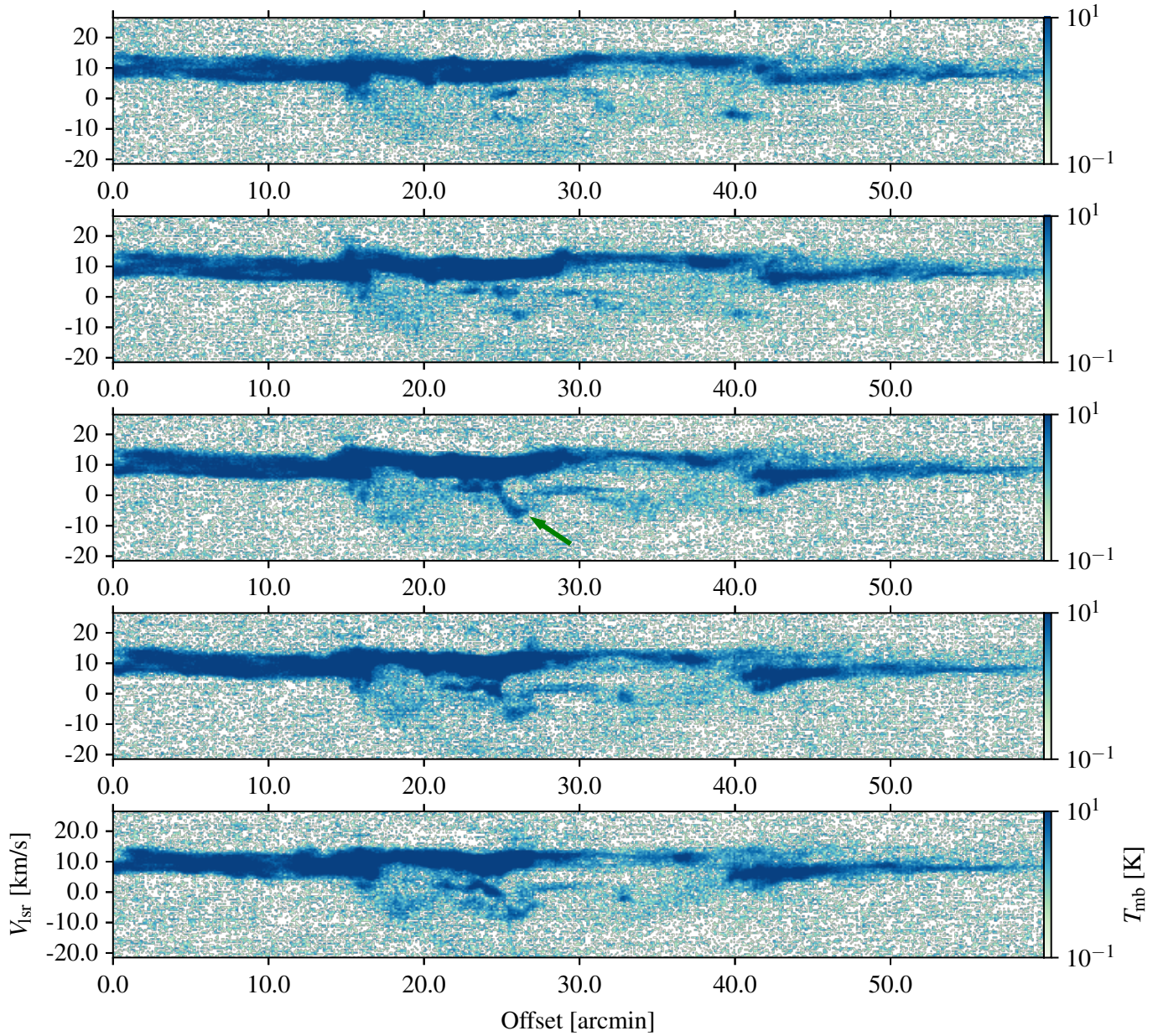


Fig. C.1: Five consecutive PV diagrams showing the changes of the dent 1. The PV diagrams cover the Veil shell from east to west, spanning 60' in length and 30'' in width. The declination of the PV diagram changes from top to bottom panel. The dent at 25' is indicated with a green arrow.

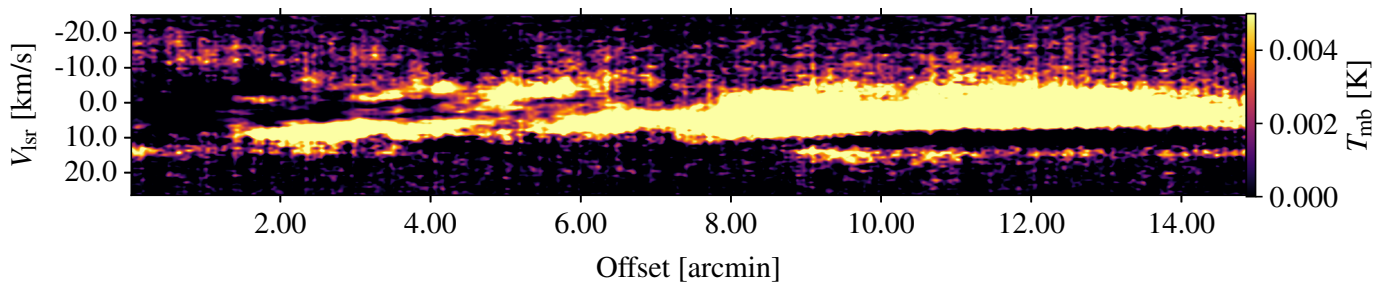


Fig. C.2: H I 21 cm PV diagram of dent 1. On Fig. C.1, the dent indicated by a green arrow is centered on the center of the PV diagram, i.e., at 7.5' in the x-axis. H I observation exists between the offset 18' and 33' in the [C II] pv-diagram in Fig. C.1.

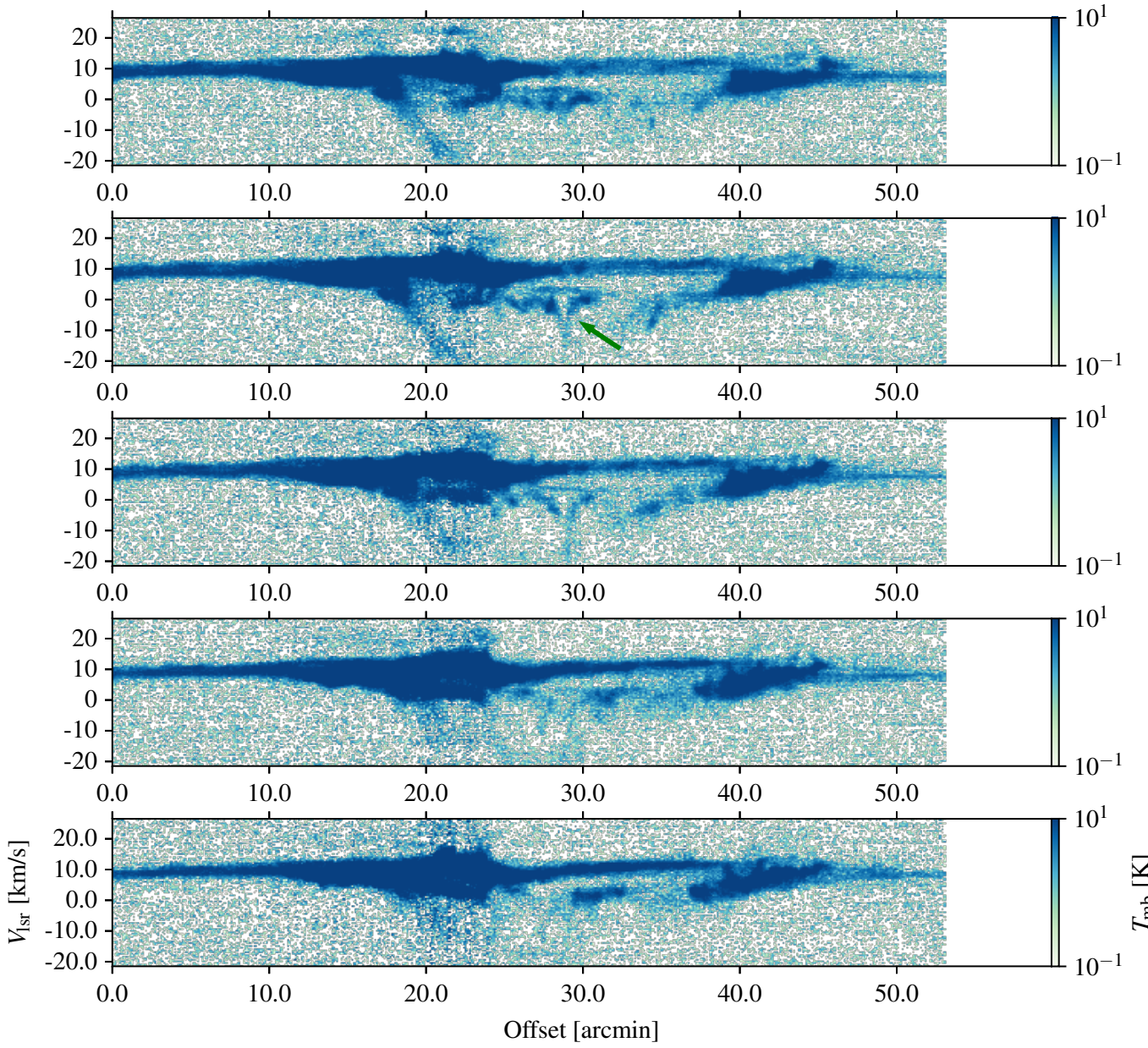


Fig. C.3: Five consecutive PV diagrams showing the changes of the dent 2. The PV diagrams cover the Veil shell from east to west, spanning 60' in length and 30'' in width. The declination of the PV diagram changes from top to bottom panel. The dent at 27' is indicated with a green arrow.

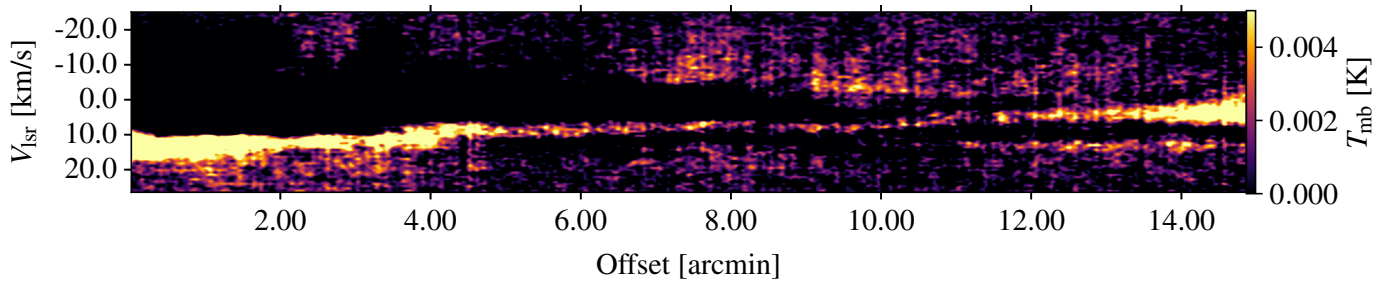


Fig. C.4: H I 21 cm PV diagram of dent 2. On Fig. C.3, the dent indicated by a green arrow is centered on the center of the PV diagram, i.e., at 7.5' in the x-axis. H I observation exists between the offset 20' and 35' in the [C II] PV-diagram in Fig. C.3.

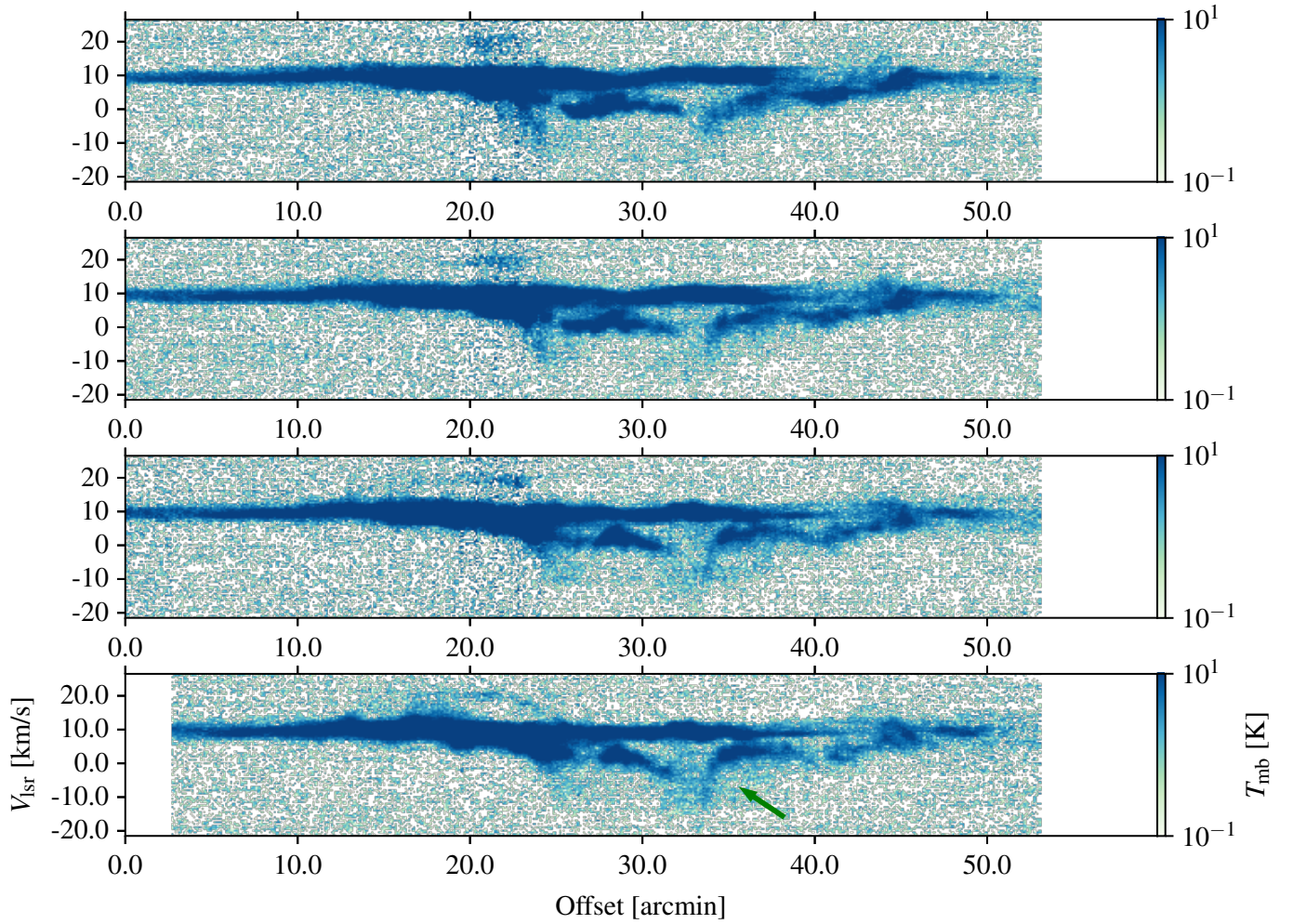


Fig. C.5: Four consecutive PV diagrams showing the changes of the dent 3. The PV diagrams cover the Veil shell from east to west, spanning 60' in length and 30'' in width. The declination of the PV diagram changes from top to bottom panel. The dent at 33' is indicated with a green arrow.

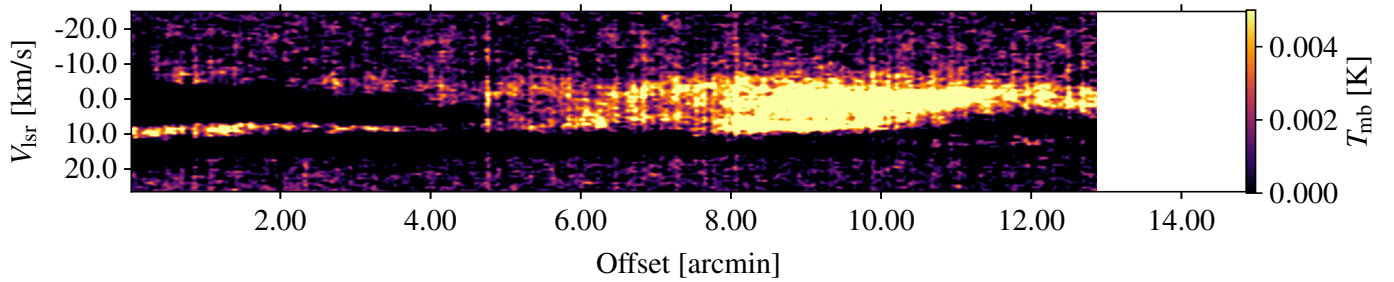


Fig. C.6: H I 21 cm PV diagram of dent 3. On Fig. C.5, the dent indicated by a green arrow is centered on the center of the PV diagram, i.e., at 7.5' in the x-axis. H I observation exists between the offset 25' and 40' in the [C II] PV-diagram in Fig. C.5.

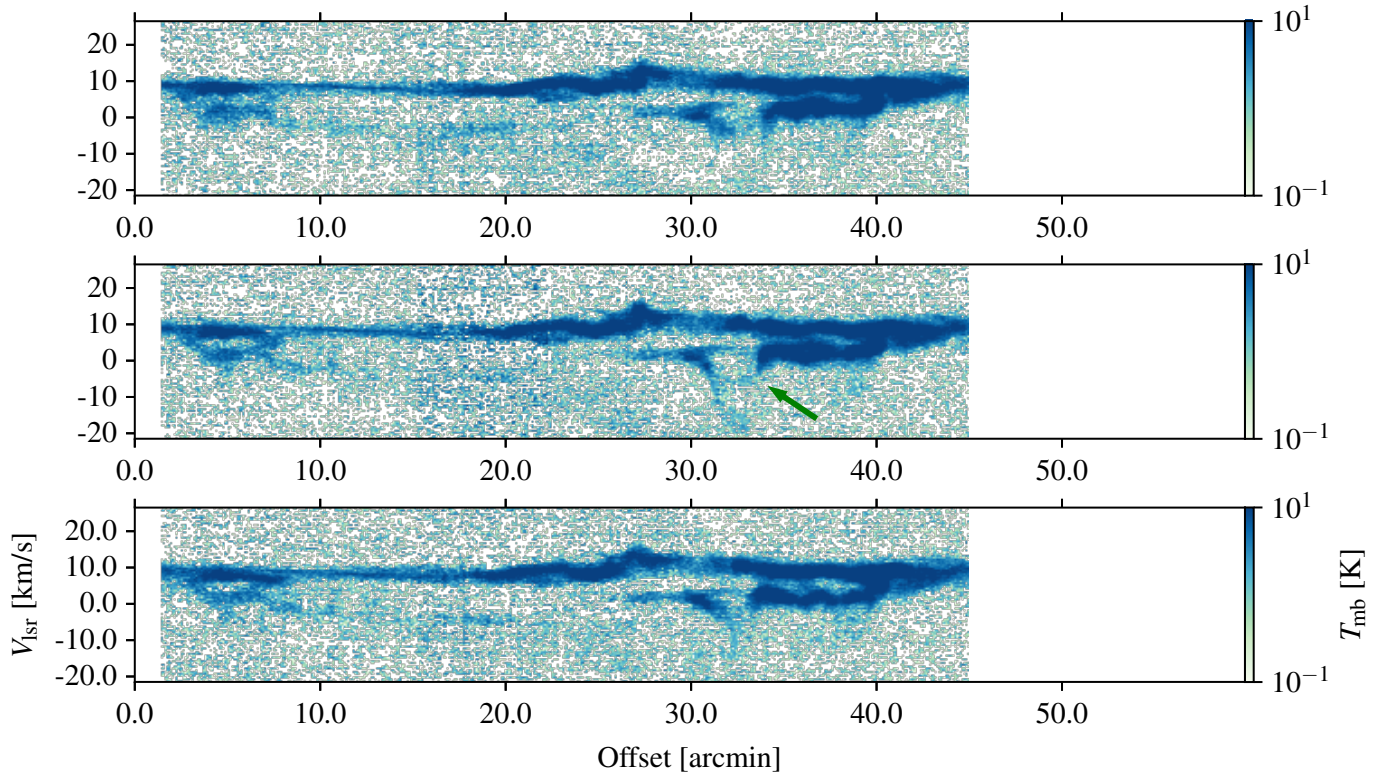


Fig. C.7: Three consecutive PV diagrams showing the changes of the dent 4. The PV diagrams cover the Veil shell from east to west, spanning $60'$ in length and $30''$ in width. The declination of the PV diagram changes from top to bottom panel. The dent at $34'$ is indicated with a green arrow.

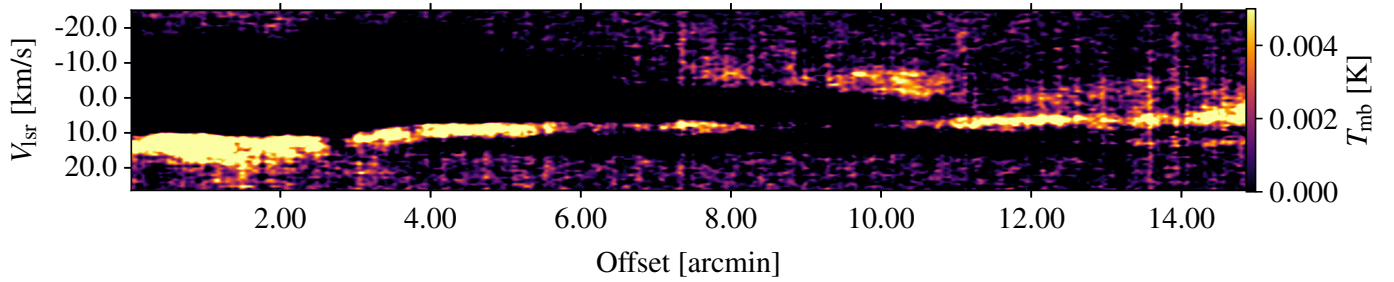


Fig. C.8: H I 21 cm PV diagram of dent 4. On Fig. C.7, the dent indicated by a green arrow is centered on the center of the PV diagram, i.e., at $7.5'$ in the x-axis. H I observation exists between the offset $25'$ and $40'$ in the [C II] PV-diagram in Fig. C.7.

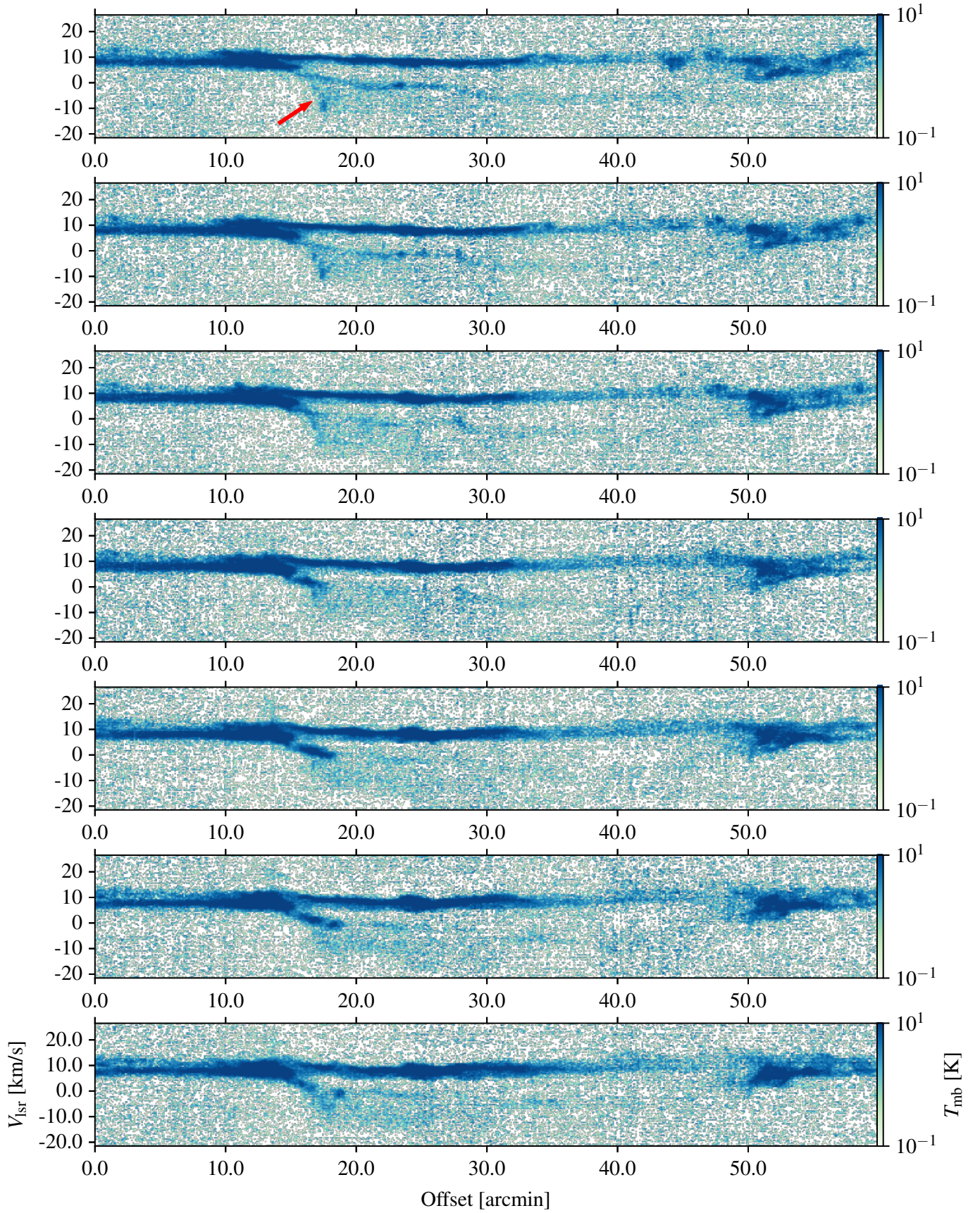


Fig. C.9: Seven consecutive PV diagrams showing the changes of the dent 5. The PV diagrams cover the Veil shell from east to west, spanning 60' in length and 30'' in width. The declination of the PV diagram changes from top to bottom panel. The dent at 18' is indicated with a red arrow.

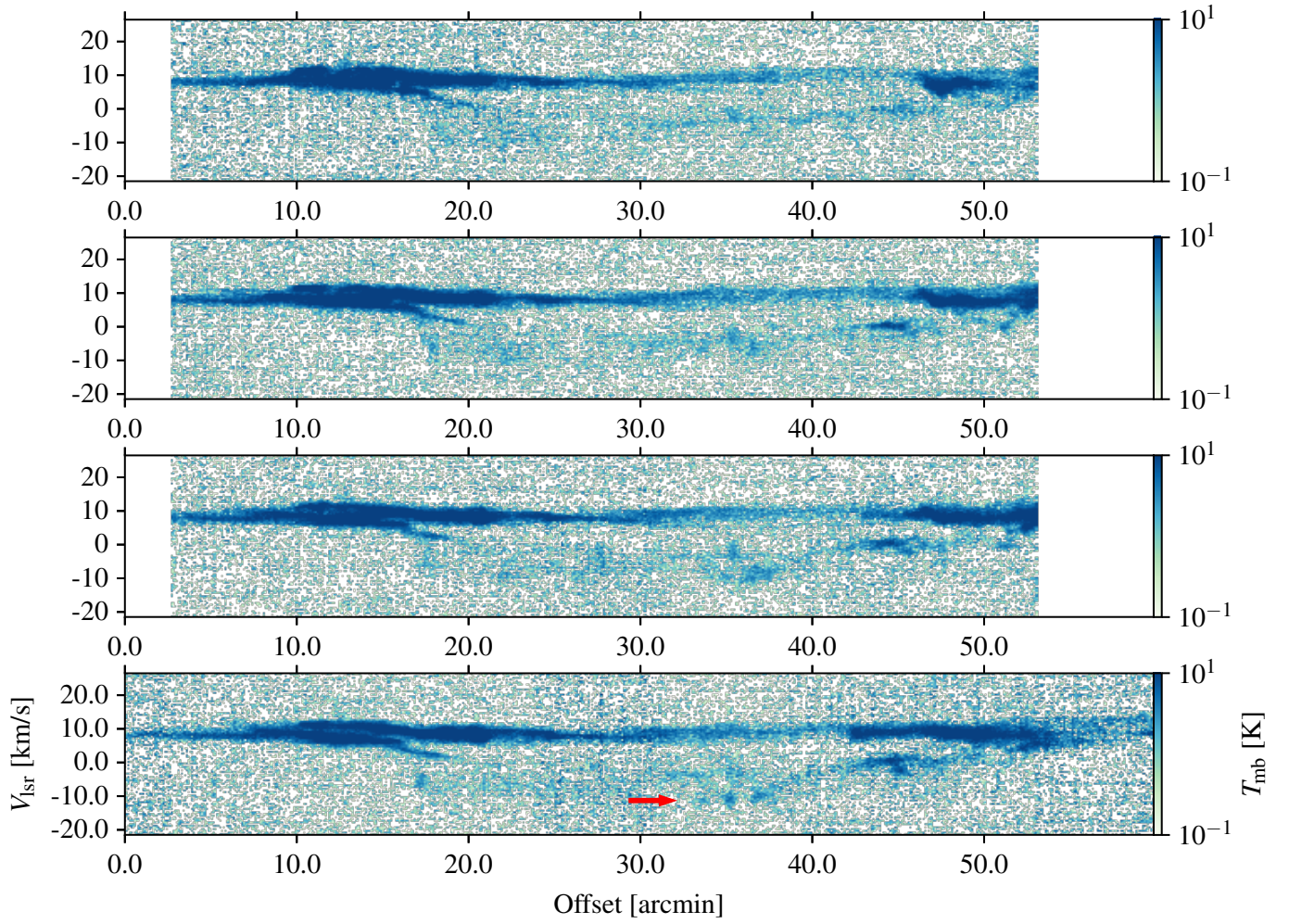


Fig. C.10: Four consecutive PV diagrams showing the changes of the dent 6. The PV diagrams cover the Veil shell from east to west, spanning 60' in length and 30'' in width. The declination of the PV diagram changes from top to bottom panel. The dent at 33' is indicated with a red arrow.

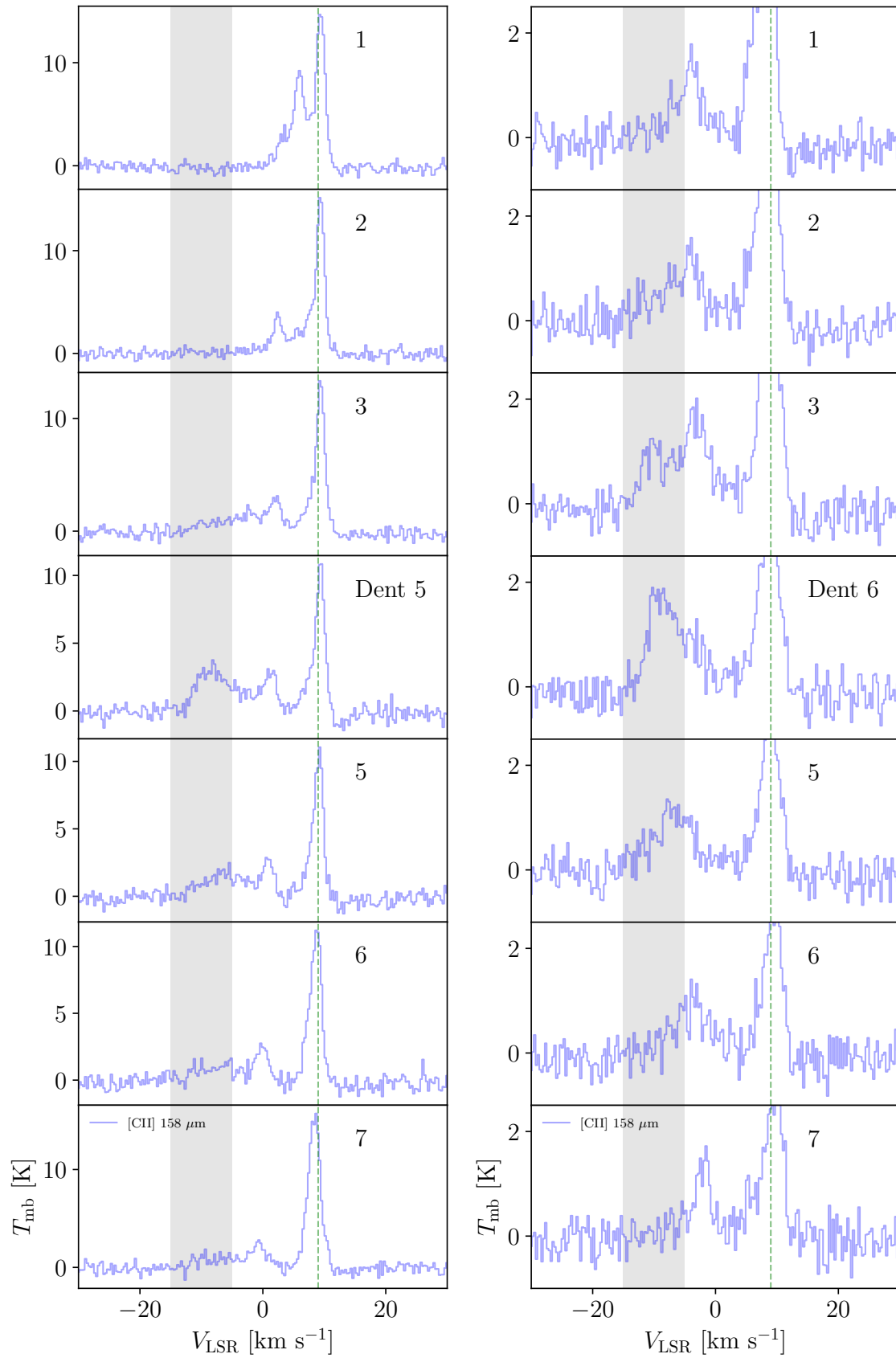


Fig. C.11: Horizontally consecutive [C II] spectra extracted over dents 5 and 6, demonstrating the change of the line profile.